ACS NANO
Cite This: ACS Nano 2019, 13, 1213−1222
www.acsnano.org

ARTICLE

Enhanced Second Harmonic Generation from Ferroelectric HfO_2-Based Hybrid Metasurfaces

Jun Qin,[†,○] Fei Huang,[†,○] Xinyue Li,[‡,#,○] Longjiang Deng,[†] Tongtong Kang,[†] Andrey Markov,[§] Fuyong Yue,[§] Yiqin Chen,[∥] Xinglin Wen,[⊥] Sheng Liu,[⊥] Qihua Xiong,[⊥] Sergey Semin,[#] Theo Rasing,[#] Daniele Modotto,[¶] Roberto Morandotti,[§,▲,△] Jialiang Xu,[*,‡] Huigao Duan,[*,∥] and Lei Bi[*,†]

[†]National Engineering Center of Electromagnetic Radiation Wave Control Materials, School of Electronic Science and Engineering, University of Electronic Science and Technology of China, Chengdu 610054, China

[‡]School of Materials Science and Engineering, National Institute for Advanced Materials, Nankai University, Tongyan Road 38, Tianjin 300350, P. R. China

[§]INRS-Énergie, Matériaux et Télécommunications, Varennes, QC G1K 9A9, Canada

[∥]College of Mechanical and Vehicle Engineering, Hunan University, Changsha 410082, China

[⊥]Division of Physics and Applied Physics, School of Physical and Mathematical Sciences, Nanyang Technological University, Singapore 637371

[#]Institute for Molecules and Materials (IMM), Radboud University, Heyendaalseweg 135, 6525AJ Nijmegen, The Netherlands

[¶]Dipartimento di Ingegneria dell'Informazione, Università di Brescia, via Branze 38, 25123 Brescia, Italy

[▲]ITMO University, St. Petersburg 197101, Russia

[△]Institute of Fundamental and Frontier Sciences, University of Electronic Science and Technology of China, Chengdu 610054, China

Supporting Information

ABSTRACT: **Integrated nonlinear metasurfaces leading to high-efficiency optical second harmonic generation (SHG) are highly desirable for optical sensing, imaging, and quantum photonic systems. Compared to traditional metal-only metasurfaces, their hybrid counterparts, where a noncentrosymmetric nonlinear photonic material is incorporated in the near-field of a metasurface, can significantly boost SHG efficiency. However, it is difficult to integrate such devices on-chip due to material incompatibilities, thickness scaling challenges, and the narrow band gaps of nonlinear optical materials. Here, we demonstrate significantly enhanced SHG in on-chip integrated metasurfaces by using nanometer thin films of ferroelectric Y:HfO_2. This material has the merit of CMOS compatibility, ultraviolet transparency up to 250 nm, and significant scalability down to sub-10 nm when deposited on silicon. We observe a 20-fold magnitude enhancement of the SHG intensity from the hybrid metasurface compared to a bare ferroelectric HfO_2 thin film. Moreover, a 3-fold SHG enhancement is observed from the hybrid metasurface compared to a control structure using nonferroelectric HfO_2, demonstrating a major contribution to the SHG signal from ferroelectric Y:HfO_2. The effective second-order nonlinear optical coefficient $\chi^{(2)}$ of Y:HfO_2 is determined to be 6.0 ± 0.5 pm/V, which is comparable to other complex nonlinear photonic oxide materials. Our work provides a general pathway to build an efficient on-chip nanophotonic nonlinear light source for SHG using ferroelectric HfO_2 thin films.**

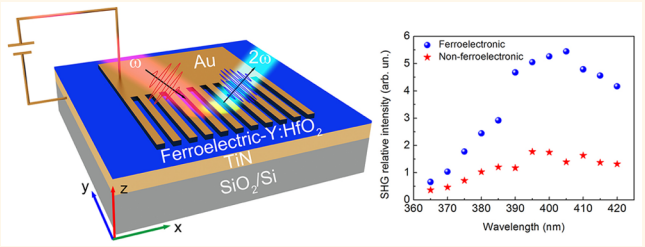

KEYWORDS: *ferroelectric Y:HfO_2, second harmonic generation, nonlinear photonics, metasurface, plasmonics*

Optical frequency conversion, commonly realized using nonlinear optical crystals, is the essence of multiple modern applications in biological science, photonics, and quantum optics. In particular, second harmonic generation (SHG) is of considerable importance in high-resolution bioimaging,[1] whereas spontaneous parametric down-conversion[2,3] and four-wave mixing[4,5] are the cornerstones of quantum technologies for entangled photon pairs and multiphoton generation. However, conventional methods for frequency conversion rely on the use of nonlinear crystals and

Received: August 19, 2018
Accepted: January 10, 2019
Published: January 10, 2019

DOI: 10.1021/acsnano.8b06308
ACS Nano 2019, 13, 1213−1222

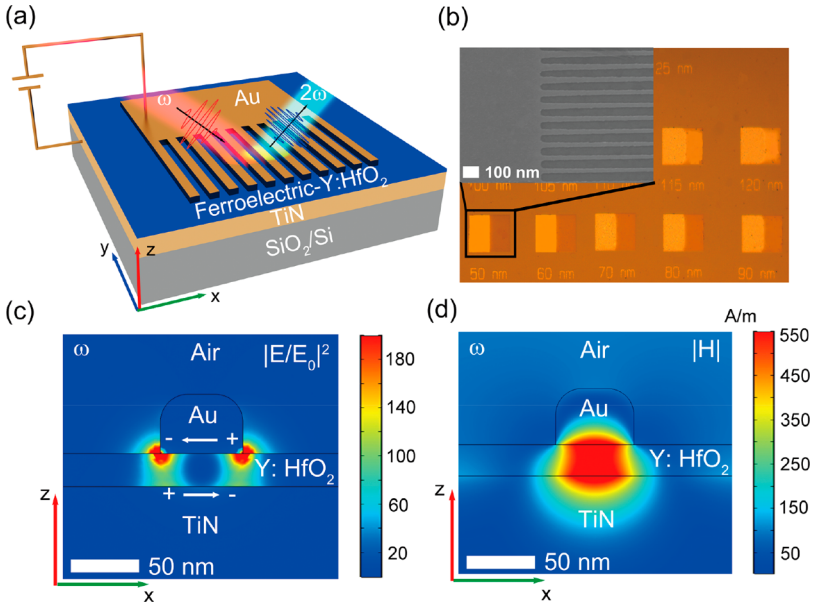

Figure 1. Device layout and field distributions. (a) Schematic of the ferroelectric Y:HfO_2-based metasurface. An electric field is applied between the bottom TiN layer and the top gold pad area to pole the ferroelectric Y:HfO_2 material. The gold grating structure can couple the fundamental frequency light into a waveguide-cavity mode to enhance the second harmonic generation of the device. (b) Optical microscope image of the Y:HfO_2-based metasurfaces featuring gold stripes of different widths. The inset is the SEM image of the 50 nm wide gold grating structure. (c) Square of the electric field distribution, normalized to the incident plane wave field amplitude, in the *xz* cutting plane at the resonance frequency of the device. The electric field is strongly localized at the two bottom corners of the gold stripes at the fundamental frequency. (d) Magnetic field distribution at the fundamental frequency.

therefore suffer from bulky sizes and complex phase-matching conditions. Nonlinear metasurfaces,[6,7] consisting of metallic or dielectric nanostructures,[8] have become a rapidly growing research topic due to their capabilities of engineering nonlinear optical processes, such as localized phase control for higher-harmonic generation,[9] as well as for their compact size. The associated local nonlinear optical response can be increased by orders of magnitude through a strong field enhancement associated with surface plasmon resonances.[10,11] Moreover, the requirement of phase-matching is totally relaxed due to the ultrathin thicknesses of metasurface-based devices. Enhanced frequency conversion efficiency, locally engineered polarization, and phase manipulation, as well as their miniature size, make nonlinear metasurfaces highly desirable for the realization of high-dimensional quantum entanglement generation that could largely expand the capabilities of current quantum systems.[12−14]

Recently, efficient nonlinear effects have been observed in a variety of nonlinear metasurface nanostructures, such as noncentrosymmetric plasmonic nanostructures, metasurfaces supporting multiresonant wavelengths, or those based on dispersive meta-atoms and providing subwavelength phase engineering.[15−17] Hybrid nonlinear metasurfaces, where a nonlinear photonic material is incorporated in the near-field of an optical nanostructure, provide a way to significantly boost nonlinear photonic effects at the nanoscale.[18−23] In previous studies, enhanced SHG has been observed in Au/$BaTiO_3$ core−shell nanocrystals,[24] Au/$KNbO_3$ hybrid nanowires,[25] ZnO nanowires on plasmonic nanostructures,[26] molecular material-based hybrid light−matter states,[27] *etc.* However, several challenges prevent on-chip integration of such hybrid nonlinear metasurfaces with standard CMOS fabrication technologies, which are important for Pockels effect-based electro-optical modulators and on-chip second harmonic generation applications. First, conventional ferroelectric materials such as $BaTiO_3$, $LiNbO_3$, and $PbTiO_3$ are not CMOS-compatible. Second, perovskite-type ferroelectric thin films ($BaTiO_3$, $LiNbO_3$, $PbTiO_3$) show significantly decreased polarization and Curie temperature for thicknesses below 10 nm[28] when deposited on silicon, limiting the scaling of hybrid nonlinear metasurfaces to smaller footprints. Third, a large optical band gap and a wide operation wavelength range are desired for SHG nonlinear photonic materials, which is around 1.4−4 eV for materials such as GaAs, ZnO, $LiNbO_3$, and $BaTiO_3$. Therefore, a CMOS-compatible, scalable, and UV-transparent ferroelectric nonlinear photonic material is highly desirable.

Recently, ferroelectric HfO_2 thin films have attracted a lot of research interest.[29−31] Although HfO_2 is conventionally a nonferroelectric material in its monoclinic phase, by forming an orthorhombic phase with the noncentrosymmetric $Pca2_1$ space group structure, room temperature ferroelectric properties can be obtained in sub-20 nm rare-earth-doped HfO_2 thin films, which is critical for a sizable second-order susceptibility (see Supporting Information Figure S1). As a widely applied high-K oxide for gate dielectrics of metal−oxide−semiconductor field-effect transistors (MOSFETs), this material is compatible with CMOS technologies. Remarkably, its room temperature ferroelectric properties can be maintained down to a film thickness of 3−5 nm, with a remanent polarization similar to that of thicker films.[32,33] Moreover, HfO_2 shows a wide band gap up to 5 eV, which can be further widened with doping.[34] These properties have ignited great research interest toward microelectronic applications, such as sub-20 nm ferroelectric memories and negative capacitance field-effect transistors.[35] However, to the best of our knowledge, there has been no report so far on using such materials for nanophotonic applications.

DOI: 10.1021/acsnano.8b06308
ACS Nano 2019, 13, 1213−1222

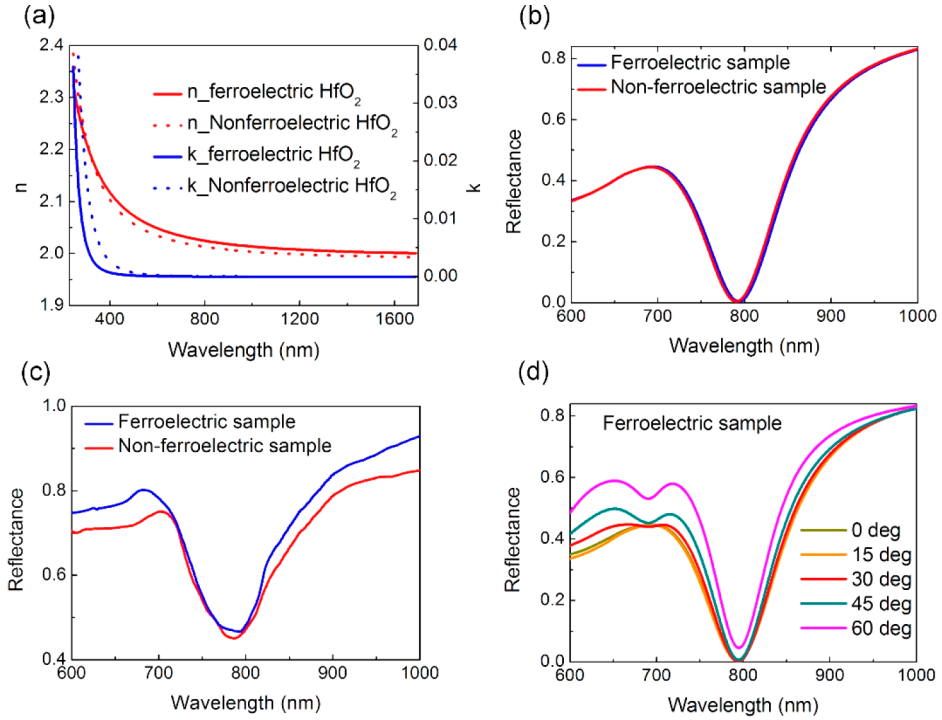

Figure 2. Linear optical properties of Y:HfO_2 thin films and devices. (a) Refractive index and extinction coefficient for both ferroelectric (solid lines) and nonferroelectric (dashed lines) Y:HfO_2 thin films measured by ellipsometry. (b) Simulated reflectance spectra for ferroelectric and nonferroelectric Y:HfO_2 metasurfaces based on the optical constants in (a). The Y:HfO_2 is 24 nm thick, the Au grating width is 50 nm, and the grating period is 240 nm. (c) Reflectance spectra for ferroelectric and nonferroelectric Y:HfO_2 devices measured at the Au grating area. (d) Simulated reflectance spectra of the ferroelectric sample with different incident angles ranging from 0 to 60°.

Here, we demonstrate an on-chip hybrid nonlinear metasurface for second harmonic generation using nanometer thick ferroelectric yttrium-doped HfO_2 thin films. The optical constant characterization indicates a band gap of 4.9 eV for these films. By incorporating a 20 nm thick noncentrosymmetric ferroelectric Y:HfO_2 thin film in a plasmonic metasurface nanocavity, we observe a 20-fold enhancement in terms of the SHG signal compared to its bare counterpart when pumped at a wavelength of 800 nm. Moreover, a 3-fold SHG enhancement is observed in hybrid metasurfaces compared to a control device using nonferroelectric HfO_2 with almost identical linear optical properties, which confirms the major contribution of SHG from ferroelectric Y:HfO_2. We have also demonstrated a good scalability in the realization of Y:HfO_2 films, that is, down to a thickness of 14 nm. We have observed an effective quadratic coefficient for polycrystalline Y:HfO_2 thin films of $\chi^{(2)}$ = 6.0 ± 0.5 pm/V, which is comparable to that of 5% MgO:$LiNbO_3$ epitaxial thin films (9.4 pm/V)[36] and UV-transparent materials such as BaB_2O_4 (4.4 pm/V).[37] These findings demonstrate the potential of using ferroelectric HfO_2 for on-chip nonlinear photonic devices and provide a general way of designing on-chip hybrid nonlinear metasurfaces with pronounced SHG for bioimaging, entangled photon generation, and holography applications.

RESULTS AND DISCUSSION

Device Layout and Operation Principles. As shown in Figure 1a, the device consists of a bottom TiN electrode (which also serves as a refractory plasmonic material[38]), a ferroelectric $Hf_{0.95}Y_{0.05}O_2$ (Y:HfO_2) thin film (10−20 nm), and a top Au plasmonic grating connected to a Au pad area, which is designed to apply a poling voltage across the Y:HfO_2 film. The ferroelectric properties of the Y:HfO_2 thin films are demonstrated using piezoelectric force microscopy (PFM) phase images as well as ferroelectric hysteresis loops, by directly probing on the Au pad (see Supporting Information Figure S2). The Y:HfO_2 layer is thin enough to support a waveguide-cavity mode[39] between the Au grating and the TiN layer. Figure 1b shows the optical microscope image of the fabricated devices with a fixed period of 240 nm and different Au grating widths ranging from 50 to 125 nm, as labeled below the devices. The inset shows a zoomed-in scanning electronic microscope (SEM) image of the 50 nm wide gold grating structure. When p-polarized light (polarization direction perpendicular to the Au grating) is incident on the metasurface under the conditions of $\arg(R) + k_0 w n_e = m\pi$ (where R is the reflection coefficient of the mode, k_0 is the free-space wave vector, w is the width of the grating, m is an integer, and n_e is the effective index of the mode), the waveguide-cavity mode[40] is excited with a strong field localization in the ferroelectric Y:HfO_2 thin film nanocavity. Such a waveguide-cavity mode is shown in Figure 1c as the numerically simulated electric field enhancement $|E|^2$ at the fundamental frequency (FF) in the device cross section (note that only one periodic unit of the grating is shown in the simulations). Strong localization of the electric field is observed at both bottom corners of the gold stripes and at the interface between the gold grating structure and the Y:HfO_2 layer, which leads to an enhancement of the field intensity up to 2 orders of magnitude at the fundamental wavelength. Notice that the electric field directions in the top gold stripes and bottom TiN thin film are along opposite directions. Such a circular electric field distribution induces a y-component magnetic field, as shown in Figure 1d. The electric

DOI: 10.1021/acsnano.8b06308
ACS Nano 2019, 13, 1213−1222

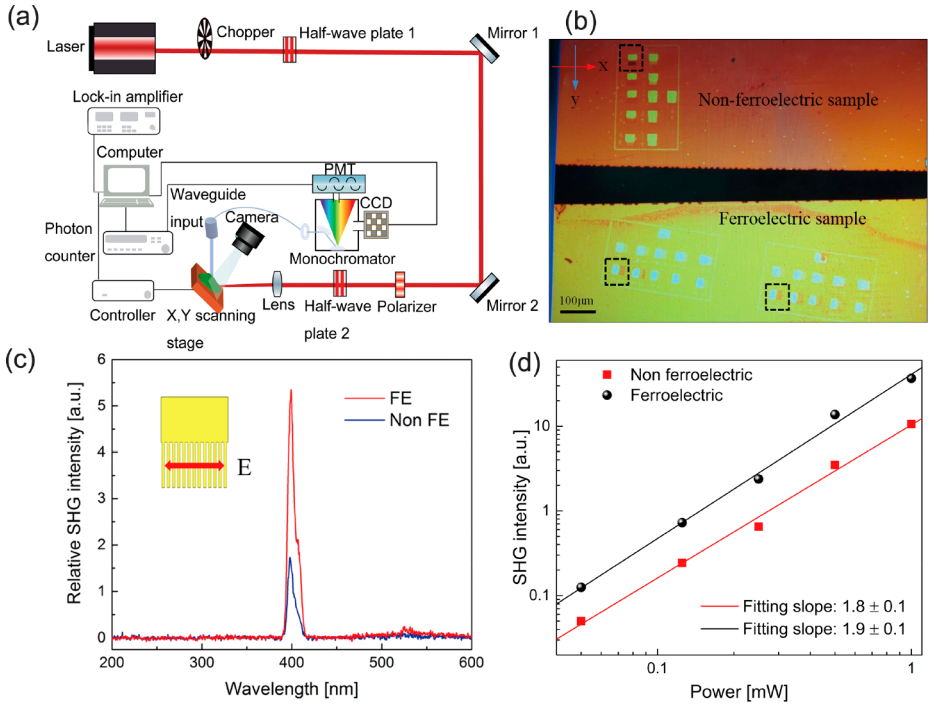

Figure 3. Experimental setup and SHG characterization. (a) Schematic presentation of the setup for SHG measurements. (b) Optical microscope image of devices with ferroelectric and nonferroelectric HfO_2 layers placed in the same field of view of the test optical microscope. (c) SHG intensity comparison between the ferroelectric and nonferroelectric sample. The polarization of the pump wave is perpendicular to the grating direction. (d) Power dependence of the SHG intensity for both the ferroelectric and nonferroelectric samples; slopes of 1.8 ± 0.1 and 1.9 ± 0.1 are observed for the two samples.

field and magnetic field distributions match with the waveguide-cavity mode characteristics.

Linear Optical Properties. The optical constants of ferroelectric Y:HfO_2 thin films have been characterized by ellipsometry (see Methods). For comparison, a 20 nm thick paraelectric HfO_2 thin film in its centrosymmetric monoclinic phase with no Y doping is also characterized, as shown in Figure 2a. First, it can be noticed that both materials show absorption edges in the ultraviolet range. Using the Tauc-plot method,[41] the optical band gaps of ferroelectric Y:HfO_2 and nonferroelectric HfO_2 are estimated to be 4.9 and 4.8 eV, respectively (Supporting Information Figure S3), which are much wider than those of $LiNbO_3$ and $BaTiO_3$ (both ~3.7 eV[42,43]). The refractive indices of both thin films are around 2.0 in the visible to near-infrared wavelength range. The slight difference between the two samples possibly originates from their different crystal structures. Using the measured optical constants, reflection spectra of both samples are simulated under normal incidence conditions, as shown in Figure 2b. The Au grating period of 240 nm and width of 50 nm are designed such that the resonant wavelength is around 800 nm. Similar reflection spectra are observed for both samples, with only a small blue shift of the nonferroelectric sample due to a slightly lower refractive index for nonferroelectric HfO_2 as shown in Figure 2a. The measured reflection spectra for both samples agree well with the simulation results (see Figure 2c). Nonetheless, a higher reflectance is observed in the experiments, which is possibly due to imperfect device dimensions and surface roughness. For SHG characterizations, the incoming light is incident at an angle of 45°, and therefore, the simulated reflectance spectra for different incident angles are also shown in Figure 2d. The excitation wavelength of the waveguide-cavity mode is almost independent of the incident angle. The field enhancement factor $F = |E|^2/|E_0|^2$ for both samples is further simulated at a 45° angle of incidence, leading to a peak F value of about 200 for both ferroelectric and nonferroelectric samples. From the above analysis, the linear optical properties of our ferroelectric and nonferroelectric devices are comparable, leading to an excited cavity mode with similar field enhancement factors at the pump wavelength.

Second Harmonic Generation from Ferroelectric HfO_2 Metasurfaces. The setup for SHG characterization is shown in Figure 3a. A Ti:sapphire laser with a pump wavelength of 760−840 nm, incident power of 10.0−15.4 mW, and incident angle of 45° is used for SHG characterization (see Methods). In order to avoid the exchange of samples and the consequent intensity measurement errors, both samples are placed side-by-side under the same field of view of the microscope, as shown in Figure 3b. The poling process for the ferroelectric samples is detailed in the Methods. Figure 3c shows the SHG spectra of the nonferroelectric and ferroelectric metasurface with p-polarized incident light normalized to the incident optical power E_0^2. Compared to the nonferroelectric sample, a 3 times higher peak SHG signal is observed in the ferroelectric metasurface. By integrating the peak area, a 3.3-fold SHG intensity enhancement is demonstrated from the ferroelectric sample with respect to the nonferroelectric one. Compared to the bare ferroelectric HfO_2 thin film on TiN, the SHG signal from the ferroelectric metasurface is about 20 time higher (see Supporting Information Figure S5). The SHG power dependence of both samples is shown in Figure 3d. A nearly quadratic relationship between the incident and emission power is observed for both samples with slopes of 1.9 ± 0.1 and 1.8 ± 0.1, respectively, confirming the SHG origin of the signals. The mapping area is 50 × 50 μm^2. For s-polarized incident light, a

DOI: 10.1021/acsnano.8b06308
ACS Nano 2019, 13, 1213−1222

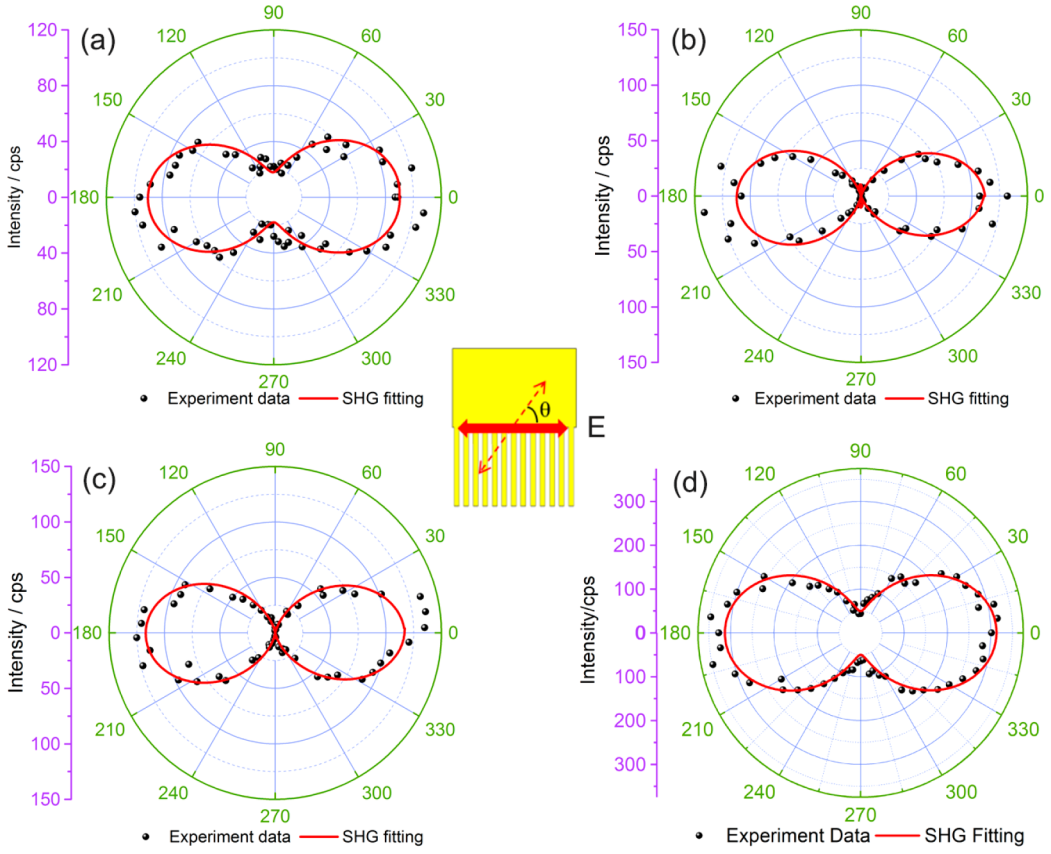

Figure 4. Nonlinear optical properties of the Y:HfO_2-based metasurface. Polarization dependence of the SHG intensity from (a) gold pads and (b) metasurface structures of the nonferroelectric sample. Polarization dependence from (c) gold pads and (d) grating structures of the ferroelectric sample. A sketch of the defined polarization direction is shown in the center. The wavelength of the incident light is 800 nm, and the power is 15.4 mW. The angle of incidence is 45°.

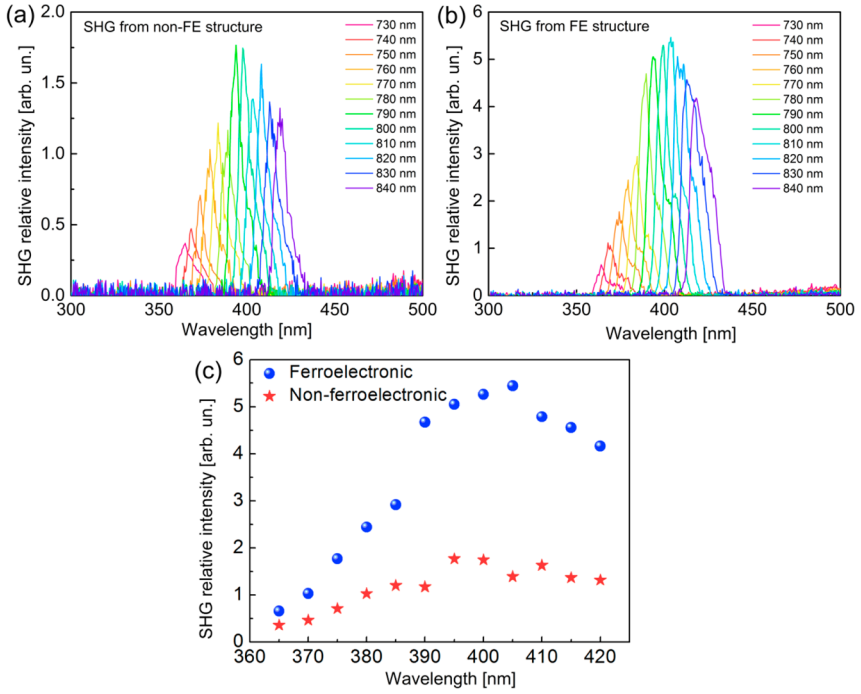

Figure 5. Wavelength-dependent SHG of the devices. Wavelength-dependent SHG spectra collected from (a) a non-ferroelectric and (b) a ferroelectric-poled sample, and (c) comparison of the SHG intensity of the samples in (a) and (b).

clear SHG signal is observed from both the Au pad and Au grating regions. The former is due to the surface susceptibility of Au under s-polarized light excitation, whereas the latter is due to the excitation of the metasurface waveguide-cavity

DOI: 10.1021/acsnano.8b06308
ACS Nano 2019, 13, 1213−1222

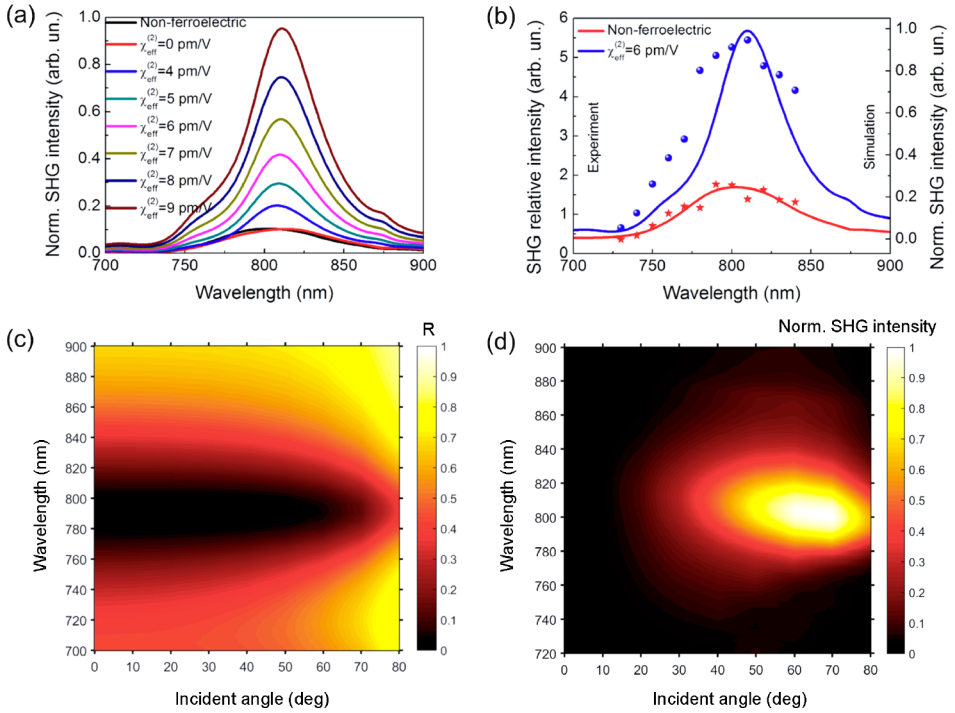

Figure 6. Numerical simulation of the SHG spectrum. (a) Simulated SHG spectra obtained by assuming different $\chi^{(2)}_{eff}$ coefficients for the ferroelectric Y:HfO_2 thin film. The SHG of the nonferroelectric sample (black curve) is shown as a reference. (b) Comparison between the experimental (dots) and simulated (continuous line) SHG spectra for both the ferroelectric and nonferroelectric samples. A good match is observed at $\chi^{(2)}_{eff}$(Y:HfO_2) = 6 pm/V. (c) Reflectance of the nonferroelectric sample as a function of the incident angle and wavelength. The low reflectivity region around 800 nm indicates the excitation of the waveguide-cavity mode. (d) Simulated SHG intensity as a function of the incident angle and wavelength for the ferroelectric sample.

mode. A full area mapping of SHG intensity for all devices has also been carried out, including 11 metasurface structures with different Au grating widths, ranging from 50 to 125 nm (Supporting Information Figure S4). The maximum SHG peak has been observed for the 50 nm grating structure with 800 nm incident light, which is in good agreement with the linear optical response shown in Figure 2b. For devices with larger grating widths, the position of the maximum SHG signal red-shifts to longer wavelengths. Therefore, for the characterization which follows, we focus on the 50 nm grating structure.

Further, Figure 4 shows the polarization dependence of the SHG intensity for both the ferroelectric and nonferroelectric samples, where θ is the polarization angle of the incident light in the sample coordinates, as shown in the figure. Figure 4a,b depicts the SHG signals recorded from the gold pad and the grating area of the ferroelectric sample, respectively. From Figure 4a, it can be seen that the intensity of SHG reaches a maximum when the polarization is near 0 or 180°, whereas it decreases to a minimum near 90 or 270°; this is due to the surface SHG susceptibility $\chi^{(2)}_{zzz}$(Au) of the gold film under p-polarized incident light.[44] The SHG signal from the gold pad and the signal recorded from the gratings have the same polarization dependence, as shown in Figure 4b. This is due to the excitation of the waveguide-cavity mode by the p-polarized light. Therefore, a $\cos^2\theta$ function can be used to fit both spectra, as indicated by the red curves in both figures, demonstrating good agreement with the experimental data. Figure 4c,d shows the SHG signals from the gold pad and grating areas of the ferroelectric-poled samples, respectively. Similar intensity profiles and polarization dependences are observed from the Au pad in both samples, indicating a similar Au quality. On the other hand, a ~3-fold enhancement of the SHG intensity is observed in Figure 4d compared to Figure 4b, confirming a stronger SHG in the ferroelectric sample.

Finally, we characterized the wavelength dependence of the device SHG spectra. The SHG intensities are normalized to the incident light intensity $|E|^2$ at each wavelength. The SHG intensities in Figure 5a,b show that the maximum SHG is observed at around 400 nm when pumped at 800 nm for both samples. This is consistent with the reflectance spectra presented in Figure 2b,c, indicating again that both samples show resonances at almost the same wavelength. To make the comparison clearer, the wavelength-dependent SHG peak intensity for both samples is plotted in Figure 5c. It shows that the SHG intensity from the ferroelectric sample is about 3 times higher than that from the nonferroelectric sample for all wavelengths. We also measured the wavelength-dependent SHG intensity of a ferroelectric device before poling (data not shown). The SHG intensity is only slightly lower (~10%) compared to the poled device on the same Y:HfO_2 sample. This is possibly due to the polycrystalline nature of the Y:HfO_2 thin film, which shows domain sizes of 20−50 nm, comparable to the field enhancement region size in Figure 1c. This result is also consistent with previous studies on randomly oriented nonlinear crystals.[45−47]

To estimate the second-order nonlinear optical susceptibility of ferroelectric Y:HfO_2 thin films, numerical simulations using a finite element method (COMSOL Multiphysics) are used to calculate the SHG spectrum. The whole simulation can be divided into three steps. First, the electric field distributions are simulated at the fundamental frequency. Then, the fundamental electric field is used to calculate the nonlinear polarization

DOI: 10.1021/acsnano.8b06308
ACS Nano 2019, 13, 1213−1222

in both the Au structure and HfO_2 film. Finally, the nonlinear polarization is defined as a source of second harmonic to calculate the generated emission in the far field. For the Au structure, only the surface $\chi^{(2)}$ coefficient ($\chi^{(2)}_{zzz}$(Au)) is contributing to the SHG.[37] Here, a classical model combined with Maxwell's equation is used to simulate the SHG of gold.[48,49] The nonlinear polarization of the Y:HfO_2 film is computed by assuming an effective $\chi^{(2)}_{eff}$ coefficient (see Supplementary Note 1). SHG from TiN is ignored due to its much smaller $\chi^{(2)}$ coefficient compared to Au[50] as well as the much lower electric field intensity in TiN, as shown in Figure 1c. To obtain an accurate device profile, the sample morphology is measured by atomic force microscopy (AFM) (see Supporting Information Figure S6). The Au grating shows rounded corners with a film thickness of 38−44 nm, which are taken into consideration in the model. The simulated SHG spectrum shows a peak at around 800 nm (see Figure 6a), corresponding to the excitation of the waveguide-cavity mode. The peak SHG intensity is almost linearly proportional to the $\chi^{(2)}_{eff}$ coefficient of Y:HfO_2. A good match between the experiments and the simulation can be observed when $\chi^{(2)}_{eff}$ is equal to 6.0 pm/V (see Figure 6b). Considering the variation of the Au film thicknesses, the simulated $\chi^{(2)}_{eff}$ is 6.0 ± 0.5 pm/V (see Supplementary Note 1). Using these parameters, the linear and nonlinear response of the device can be evaluated in the full parameter space. Figure 6c,d shows the simulations of the reflectance and SHG intensity of the device as a function of the incident wavelength and angles, respectively. From Figure 6c, we observe that the waveguide-cavity mode, for wavelengths around 800 nm, can be excited under a wide range of angles. However, the SHG intensity shows a stronger dependence on the incident angles. Simple numerical simulations have suggested that the reason for the strong angular dependence of SHG must be sought in the correlation between the incident angle and the field distribution in the Y:HfO_2 layer (and, in particular, near the interface with gold). A maximum SHG intensity can be observed at around 65°, which is 31.7% higher compared to the case of 45°, as presented in Figure 6b.

In this work, we report second harmonic generation in ferroelectric HfO_2-based metasurfaces. The possibility of scaling ferroelectric Y:HfO_2 to 20 nm or a thinner thickness is crucial for the enhancement of SHG in such hybrid metasurfaces. To demonstrate this, numerical simulations have been performed by varying the HfO_2 thicknesses and $\chi^{(2)}_{eff}$ values with the same Au grating period and device structure, as shown in the Supporting Information Figure S7. The fundamental frequency gradually blue-shifts with increasing film thickness, which is consistent with the waveguide-cavity mode of the device. A higher-order mode at the SHG frequency can also be excited when the HfO_2 thickness is larger than 30 nm. More importantly, the SHG intensity is much less influenced by the thickness of the nonlinear HfO_2 film with increasing thickness, due to a much lower field intensity in HfO_2 for thicker devices. This is consistent with previous reports of SHG in plasmonic antenna coupled hybrid nonlinear photonic devices.[51,52] However, when reducing the film thickness, the field intensity quickly increases in the thin film, leading to a significant contribution of SHG from the nonlinear medium.[19] It should be noted that, in the reported device, the thickness of the ferroelectric Y:HfO_2 thin film is 24 nm. It is possible to scale this thickness further down to 10 nm or lower in the current device structure, which may yield even stronger field enhancement and higher SHG. This is demonstrated in another sample featuring a 14 nm Y:HfO_2 film thickness, as shown in Supporting Information Figure S8. Despite a spectrum red shift to 850 nm, a twice higher value of SHG is observed in this sample as compared to the 24 nm Y:HfO_2 thick film, demonstrating the potential of realizing even stronger nonlinear light sources at the nanoscale. (Due to a much weaker incident light signal at longer wavelengths, in the manuscript we focused the characterization on the 24 nm sample.) As proved by additional simulations (not reported here), further decreasing the Y:HfO_2 film thickness down to 5 nm can enhance the SHG intensity by an order of magnitude. Indeed, ferroelectricity has been reported in a 3 nm thick HfO_2 thin film on silicon,[32] which ensures further decreasing of the film thickness and enhancing of the SHG efficiency, toward a large-scale CMOS integration of nonlinear photonic light sources.

It is worth comparing the nonlinear optical coefficient of Y:HfO_2 with other ferroelectric oxides. 5% MgO-doped lithium niobate (MgO:LN) and barium titanate (BTO) show $\chi^{(2)}$ values of 9.4 and 5.5−14.4 pm/V, respectively.[36,53] On the other hand, a wide band gap nonlinear photonic material such as BaB_2O_4 (BBO, E_g = 6.0 eV) has a $\chi^{(2)}$ value of 4.4 pm/V. Therefore, Y:HfO_2 shows a $\chi^{(2)}_{eff}$ value similar to that of these materials. However, in this work, we assumed that Y:HfO_2 is polycrystalline with no preferential orientation, as is clear from X-ray diffraction (XRD) characterization. Growing epitaxial Y:HfO_2 thin films may further improve its nonlinear optical properties along certain crystalline orientations.[54] Characterization of other ferroelectric HfO_2 thin films such as Si:HfO_2 or Zr:HfO_2 may also reveal higher $\chi^{(2)}_{eff}$ values. Another advantage of ferroelectric HfO_2 is its 3D integration capability. Using atomic layer deposition (ALD), it is possible to fill deep trenches with ferroelectric HfO_2, therefore enabling the realization of 3D nonlinear photonic devices.[55] These advantages make ferroelectric HfO_2 highly versatile and attractive for different kinds of nonlinear optical metasurface nanostructures.

CONCLUSIONS

In summary, strong second harmonic generation is reported in ferroelectric Y:HfO_2-based hybrid nonlinear optical metasurfaces. A 3-fold enhancement of SHG at an incident wavelength of 800 nm is observed in ferroelectric Y:HfO_2 compared to nonferroelectric HfO_2-based devices, indicating a significant contribution of SHG from the noncentrosymmetric Y:HfO_2 material. By further scaling Y:HfO_2 down to 14 nm, an additional 2-fold enhancement for SHG is observed in such devices. An optical band gap of 4.9 eV is measured in ferroelectric Y:HfO_2. An effective second-order susceptibility $\chi^{(2)}_{eff}$ value of 6.0 ± 0.5 pm/V is estimated in the Y:HfO_2 thin films. The wide optical band gap, ultrathin film thickness, and CMOS compatibility make ferroelectric HfO_2 an attractive candidate to significantly boost the optical nonlinearity in a variety of nanophotonic devices.

METHODS

TiN and Ferroelectric Y:HfO_2 Thin Film Deposition. TiN thin films (120 nm thick) were first deposited by DC sputtering from a TiN ceramic target (Alfa Aesar, purity 99.99%) as bottom electrodes on a Si(100) substrate, capped with a 500 nm SiO_2 thermal oxide layer. The substrate was heated to 300 °C, and the deposition rate was 0.5 nm/s. Y:HfO_2 thin films were subsequently deposited at 200 °C

DOI: 10.1021/acsnano.8b06308
ACS Nano 2019, 13, 1213−1222

by PLD from a HfO_2 ceramic target (Alfa Aesar, purity 99.99%) and a Y_2O_3 ceramic target (Alfa Aesar, purity 99.99%), with a target−substrate distance of 5.5 cm, a fluence of 2 J/cm^2, and a pulse rate of 5 Hz for the HfO_2 target and 2 Hz for the Y_2O_3 target. The vacuum chamber was pumped down to a base pressure of 2×10^{-5} Pa. During deposition, the O_2 flux was fixed at 10 sccm, and the chamber pressure was maintained at pO_2 = 1 Pa. After the deposition of the Y:HfO_2 films, a 30 nm thick TiN top electrode layer was deposited *in situ* by PLD at 200 °C. Crystallization of the as-deposited amorphous Y:HfO_2 thin films was carried out by means of an *ex situ* rapid thermal annealing process. The ramp rate was 20 °C/s, up to 600 °C for 1 min before being cooled. Then, the top TiN layer was etched *via* a H_2O_2 solution (Alfa Aesar, purity 29−32%) at 70 °C. More details about the fabrication process can be found in our previous work.[14]

Metasurface Fabrication. The Au metasurface structures were fabricated by electron beam lithography (EBL, Raith 150-TWO). First, poly(methyl methacrylate) resist was spin-coated on the Y:HfO_2 film with a spin speed of 4000 rpm and baked for 5 min at 180 °C on a hot plate. Then, the metasurface structure was patterned by EBL using an accelerating voltage of 30 kV and an average dose of 270 μC/cm^2. After exposure, the samples were developed in a mixed solution of 3:1 isopropyl alcohol (IPA)/methyl isobutyl ketone for 1 min and rinsed in deionized water for 1 min. After that, a bilayer of 5 nm Ti and 30 nm Au was deposited by way of an electron beam evaporator (Kurt J. Lesker, Lab-line) at room temperature. Finally, the samples were lifted off in an acetone solution with ultrasonic cleaning and rinsed in IPA.

Electrical and Optical Measurement. The crystal structure of the Y:HfO_2 films was analyzed using an X-ray diffractometer (XRD-7000, SHIMADZU) in a $\omega-2\theta$ scan with a scanning rate of 0.5°/min. The samples for cross-sectional scanning transmission electron microscopy investigation were prepared by a dual beam focused ion beam system (Quanta 3D, FEG). PFM and AFM measurements were done on a Cypher ES Environmental AFM system. For the polarization−electric field hysterisis loop measurements, triangular positive or negative pulses were supplied by a pulse generator unit (4220-PGU, Keithley) with a pulse period of 500 μs and a pulse amplitude of 6 V. The switching current was monitored by using a remote amplifier/switch (4225-RPM, Keithley). The dielectric constant−electric field (ε_r-E) characteristics were measured using a semiconductor device analyzer (B1500A, Agilent, at the AC bias frequency of 50 kHz and amplitude of 30 mV).

For the nonlinear optical measurements, a high repetition rate (82 MHz) femtosecond laser (MaiTai, NewPort-Spectra Physics, 720−990 nm, 120 fs) was used as a pump.[57] The SHG mappings were obtained by raster scanning the SHG signal at half the wavelength of the pump at a given polarization. The polarization of the input laser was changed by using a half-wave plate, whereas the power was controlled with a combination of half-wave plate and Glan-prism polarizer. A color filter BG39 (Schott glass) and photomultiplier tube were employed to investigate the SHG polarization dependence at 800 nm excitation wavelength, which was detected with high spectral resolution *via* a SpectraPro spectrometer and a liquid nitrogen cooled charge-coupled device detector (Princeton Instruments).

Numerical Simulation. A finite element method was used to simulate the reflectance spectra and near-field modal profiles with a commercial software (COMSOL Multiphysics). A two-dimensional (2D) model of the wave optics module was used to simulate the periodic grating structure. Both the linear and nonlinear processes were calculated in one model. The permittivity of Au used in the experimental data was taken from ref 56, whereas that for TiN was fitted using the Drude-Lorentz dispersion model.[56] The optical constants of ferroelectric Y:HfO_2 and nonferroelectric HfO_2 thin films were measured using a J.A. Woollam RC2 ellipsometer with an incident angle of 60° and a wavelength range of 245−1680 nm. The linear optical response was simulated using a port boundary condition with perfect matched layers on the top and bottom boundaries of the metasurface, whereas periodic boundary conditions were used along the x direction. The period was set to 240 nm.

For SHG simulations, the field distributions at the fundamental frequency under a plane wave excitation were first simulated. Then, the fundamental field was used to calculate the nonlinear polarization, which in turn was used as the source to simulate the propagation of the second harmonic. For Au, a classical electrodynamic model was used to describe the nonlinear conversion (see Supplementary Note 1 for details). A weak contribution term was used to simulate the second harmonic generation, as indicated in eq 6 of Supplementary Note 1. The nonlinear polarization for ferroelectric Y:HfO_2 was defined as $P_z(2\omega) = \varepsilon_0\chi^{(2)}_{\mathrm{eff}}E^2_z(\omega)$, and the nonlinear equivalent current source was calculated by means of $J(r,2\omega) = \partial P(r,2\omega)/\partial t$. The far-field second harmonic power was calculated by integrating the intensity flowing through the COMSOL simulation port.

ASSOCIATED CONTENT

Supporting Information

The Supporting Information is available free of charge on the ACS Publications website at DOI: 10.1021/acsnano.8b06308.

Crystal structure of orthorhombic and monoclinic HfO_2, TEM images, XRD patterns, polarization hysteresis, PFM phase images of ferroelectric Y:HfO_2, Tauc-plot fitting of the band gap of Y:HfO_2, SHG intensity mapping of the ferroelectric Y:HfO_2 metasurface, background SHG signal of the ferroelectric and nonferoelectric Y:HfO_2 thin films, AFM images of the Au gratings, simulated SHG intensity for different Y:HfO_2 film thicknesses, wavelength-dependent SHG measured from the metasurface with a 14 nm Y:HfO_2 thin film, simulation process of the nonlinear optical susceptibility of Y:HfO_2 (PDF)

AUTHOR INFORMATION

Corresponding Authors

*E-mail: jialiang.xu@nankai.edu.cn.
*E-mail: duanhg@hnu.edu.cn.
*E-mail: bilei@uestc.edu.cn.

ORCID

Fei Huang: 0000-0001-9932-7692
Yiqin Chen: 0000-0003-4635-0666
Qihua Xiong: 0000-0002-2555-4363
Jialiang Xu: 0000-0003-2441-4809
Huigao Duan: 0000-0002-7016-6343
Lei Bi: 0000-0002-2698-2829

Author Contributions

○J.Q., F.H., and X.L. contributed equally to this work.

Notes

The authors declare no competing financial interest.

ACKNOWLEDGMENTS

Financial support from the National Natural Science Foundation of China (51522204, 61475031, 21773168, and 51503143), the Ministry of Science and Technology of China MOST (2016YFA0300802), "111 Project" of China (B18011), Netherlands Organization for Scientific Research (NWO) with the Veni Grant (680-47-437), Royal Netherlands Academy of Arts and Sciences (KNAW) with the China-Exchange Program (530-4CDP02), NSERC in Canada, the ITMO Fellowship and Professorship Program (Grant 074-U01) from the Government of the Russian Federation, and the 1000 Talents Sichuan Program in China are acknowledged.

DOI: 10.1021/acsnano.8b06308
ACS Nano 2019, 13, 1213−1222

REFERENCES

(1) Campagnola, P. J.; Loew, L. M. Second-harmonic Imaging Microscopy for Visualizing Biomolecular Arrays in Cells, Tissues and Organisms. *Nat. Biotechnol.* **2003**, *21*, 1356−1360.

(2) Arlt, J.; Dholakia, K.; Allen, L.; Padgett, M. J. Parametric Down-conversion for Light Beams Possessing Orbital Angular Momentum. *Phys. Rev. A: At., Mol., Opt. Phys.* **1999**, *59*, 3950−3952.

(3) Kwiat, P. G.; Mattle, K.; Weinfurter, H.; Zeilinger, A.; Sergienko, A. V.; Shih, Y. New High-intensity Source of Polarization-entangled Photon Pairs. *Phys. Rev. Lett.* **1995**, *75*, 4337−4341.

(4) Reimer, C.; Kues, M.; Roztocki, P.; Wetzel, B.; Grazioso, F.; Little, B. E.; Chu, S. T.; Johnston, T.; Bromberg, Y.; Caspani, L.; et al. Generation of Multiphoton Entangled Quantum States by Means of Integrated Frequency Combs. *Science* **2016**, *351*, 1176−1180.

(5) Kues, M.; Reimer, C.; Roztocki, P.; Cortés, L. R.; Sciara, S.; Wetzel, B.; Zhang, Y.; Cino, A.; Chu, S. T.; Little, B. E.; et al. On-chip Generation of High-dimensional Entangled Quantum States and Their Coherent Control. *Nature* **2017**, *546*, 622−626.

(6) Li, G.; Zhang, S.; Zentgraf, T. Nonlinear Photonic Metasurfaces. *Nat. Rev. Mater.* **2017**, *2*, 17010.

(7) Krasnok, A.; Tymchenko, M.; Alù, A. Nonlinear Metasurfaces: a Paradigm Shift in Nonlinear Optics. *Mater. Today* **2018**, *21*, 8−21.

(8) Shcherbakov, M. R.; Neshev, D. N.; Hopkins, B.; Shorokhov, A. S.; Staude, I.; Melik-Gaykazyan, E. V.; Decker, M.; Ezhov, A. A.; Miroshnichenko, A. E.; Brener, I.; et al. Enhanced Third-harmonic Generation in Silicon Nanoparticles Driven by Magnetic Response. *Nano Lett.* **2014**, *14*, 6488−6492.

(9) Li, G.; Chen, S.; Pholchai, N.; Reineke, B.; Wong, P. W.; Pun, E. Y.; Cheah, K. W.; Zentgraf, T.; Zhang, S. Continuous Control of the Nonlinearity Phase for Harmonic Generations. *Nat. Mater.* **2015**, *14*, 607−612.

(10) Schuller, J. A.; Barnard, E. S.; Cai, W.; Jun, Y. C.; White, J. S.; Brongersma, M. L. Plasmonics for Extreme Light Concentration and Manipulation. *Nat. Mater.* **2010**, *9*, 193−204.

(11) Kim, S.; Jin, J.; Kim, Y. J.; Park, I. Y.; Kim, Y.; Kim, S. W. High-harmonic Generation by Resonant Plasmon Field Enhancement. *Nature* **2008**, *453*, 757−760.

(12) Tame, M. S.; McEnery, K. R.; Özdemir, S. K.; Lee, J.; Maier, S. A.; Kim, M. S. Quantum Plasmonics. *Nat. Phys.* **2013**, *9*, 329−340.

(13) Wang, K.; Titchener, J. G.; Kruk, S. S.; Xu, L.; Chung, H. P.; Parry, M.; Kravchenko, I. I.; Chen, Y. H.; Solntsev, A. S.; Kivshar, Y. S.; et al. Quantum Metasurface for Multi-photon Interference and State Reconstruction. *Science* **2018**, *361*, 1104−1108.

(14) Fickler, R.; Lapkiewicz, R.; Plick, W. N.; Krenn, M.; Schaeff, C.; Ramelow, S.; Zeilinger, A. Quantum Entanglement of High Angular Momenta. *Science* **2012**, *338*, 640−643.

(15) Martin, J. F.; Brevet, P.; Butet, J. Optical Second Harmonic Generation in Plasmonic Nanostructures: From Fundamental Principles to Advanced Applications. *ACS Nano* **2015**, *9*, 10545−10562.

(16) Canfield, B. K.; Husu, H.; Laukkanen, J.; Bai, B.; Kuittinen, M.; Turunen, J.; Kauranen, M. Local Field Asymmetry Drives Second-harmonic Generation in Noncentrosymmetric Nanodimers. *Nano Lett.* **2007**, *7*, 1251−1255.

(17) Celebrano, M.; Wu, X.; Baselli, M.; Groβmann, S.; Biagioni, P.; Locatelli, A.; De Angelis, C.; Cerullo, G.; Osellame, R.; Hecht, B.; et al. Mode Matching in Multiresonant Plasmonic Nanoantennas for Enhanced Ssecond Harmonic Generation. *Nat. Nanotechnol.* **2015**, *10*, 412−417.

(18) Lehr, D.; Reinhold, J.; Thiele, I.; Hartung, H.; Dietrich, K.; Menzel, C.; Pertsch, T.; Kley, E. B.; Tünnermann, A. Enhancing Second Harmonic Generation in Gold Nanoring Resonators Filled with Lithium Niobate. *Nano Lett.* **2015**, *15*, 1025−1030.

(19) Chen, P. Y.; Argyropoulos, C.; D'Aguanno, G.; Alù, A. Enhanced Second-harmonic Generation by Metasurface Nanomixer and Nanocavity. *ACS Photonics* **2015**, *2*, 1000−1006.

(20) Wen, X.; Xu, W.; Zhao, W.; Khurgin, J. B.; Xiong, Q. Plasmonic Hot Carriers-Controlled Second Harmonic Generation in WSe_2 Bilayers. *Nano Lett.* **2018**, *18*, 1686−1692.

(21) Wen, X.; Li, G.; Gu, C.; Zhao, J.; Wang, S.; Jiang, C.; Palomba, S.; Martijn de Sterke, S.; Xiong, Q. Doubly Enhanced Second Harmonic Generation through Structural and Epsilon-near-Zero Resonances in TiN Nanostructures. *ACS Photonics* **2018**, *5*, 2087−2093.

(22) Liu, X.; Zhang, Q.; Chong, W. K.; Yip, J. N.; Wen, X.; Li, Z.; Wei, F.; Yu, G.; Xiong, Q.; Sum, T. C. Cooperative Enhancement of Second-Harmonic Generation from a Single CdS Nanobelt-Hybrid Plasmonic Structure. *ACS Nano* **2015**, *9*, 5018−5026.

(23) Wen, X.; Xiong, Q. A Large Scale Perfect Absorber and Optical Switch Based on Phase Change Material ($Ge_2Sb_2Te_5$) Thin Film. *Science China Materials* **2016**, *59*, 165−172.

(24) Pu, Y.; Grange, R.; Hsieh, C.; Psaltis, D. Nonlinear Optical Properties of Core-Shell Nanocavities for Enhanced Second-Harmonic Generation. *Phys. Rev. Lett.* **2010**, *104*, 207402.

(25) Richter, J.; Steinbrück, A.; Zilk, M.; Sergeyev, A.; Pertsch, T.; Tünnermann, A.; Grange, R. Core−shell Potassium Niobate Nanowires for Enhanced Nonlinear Optical Effects. *Nanoscale* **2014**, *6*, 5200−5207.

(26) Grinblat, G.; Rahmani, M.; Cortes, E.; Caldarola, M.; Comedi, D.; Maier, S.; Bragas, A. V. High-efficiency Second Harmonic Generation from a Single Hybrid ZnO Nanowire/Au Plasmonic Nano-oligomer. *Nano Lett.* **2014**, *14*, 6660−6665.

(27) Chervy, T.; Xu, J.; Duan, Y.; Wang, C.; Mager, L.; Frerejean, M.; Münninghoff, J. A. W.; Tinnemans, P.; Hutchison, J. A.; Genet, C.; Rowan, A. E.; Rasing, T.; Ebbesen, T. W. High-Efficiency Second-Harmonic Generation from Hybrid Light-Matter States. *Nano Lett.* **2016**, *16*, 7352−7356.

(28) Ihlefeld, J. F.; Harris, D. T.; Keech, R.; Jones, J. L.; Maria, J.; Trolier-Mckinstry, S. Scaling Effects in Perovskite Ferroelectrics: Fundamental Limits and Process-structure-property Relations. *J. Am. Ceram. Soc.* **2016**, *99*, 2537−2557.

(29) Böscke, T. S.; Müller, J.; Bräuhaus, D.; Schröder, U.; Böttger, U. Ferroelectricity in Hafnium Oxide Thin Films. *Appl. Phys. Lett.* **2011**, *99*, 102903.

(30) Huang, F.; Chen, X.; Liang, X.; Qin, J.; Zhang, Y.; Huang, T.; Wang, Z.; Peng, B.; Zhou, P.; Lu, H.; Zhang, L.; Deng, L.; Liu, M.; Liu, Q.; Tian, H.; Bi, L. Fatigue Mechanism of Yttrium-doped Hafnium Oxide Ferroelectric Thin Films Fabricated by Pulsed Laser Deposition. *Phys. Chem. Chem. Phys.* **2017**, *19*, 3486−3497.

(31) Müller, J.; Böscke, T. S.; Schröder, U.; Mueller, S.; Bräuhaus, D.; Böttger, U.; Frey, L.; Mikolajick, T. Ferroelectricity in Simple Binary ZrO_2 and HfO_2. *Nano Lett.* **2012**, *12*, 4318−4323.

(32) Tian, X.; Shibayama, S.; Nishimura, T.; Yajima, T.; Migita, S.; Toriumi, A. Evolution of Ferroelectric HfO_2 in Ultrathin Region Down to 3 nm. *Appl. Phys. Lett.* **2018**, *112*, 102902.

(33) Chernikova, A.; Kozodaev, M.; Markeev, A.; Negrov, D.; Spiridonov, M.; Zarubin, S.; Bak, O.; Buragohain, P.; Lu, H.; Suvorova, E.; Gruverman, A.; Zenkevich, A. Ultrathin $Hf_{0.5}Zr_{0.5}O_2$ Ferroelectric Films on Si. *ACS Appl. Mater. Interfaces* **2016**, *8*, 7232−7237.

(34) Broqvist, P.; Pasquarello, A. Band Gaps and Dielectric Constants of Amorphous Hafnium Silicates: a First-principles Investigation. *Appl. Phys. Lett.* **2007**, *90*, No. 082907.

(35) Hoffmann, M.; Pešić, M.; Chatterjee, K.; Khan, A. I.; Salahuddin, S.; Slesazeck, S.; Schroeder, U.; Mikolajick, T. Direct Observation of Negative Capacitance in Polycrystalline Ferroelectric. *Adv. Funct. Mater.* **2016**, *26*, 8643−8649.

(36) Pavel, N.; Shoji, I.; Taira, T.; Mizuuchi, K.; Morikawa, A.; Sugita, T.; Yamamoto, K. High-Power Green Generation at Room Temperature in a Periodically Poled MgO: LiNbO3 by Frequency Doubling of A Diode End-pumped Nd: GdVO4 Laser; *Proceedings of Advanced Solid-State Photonics*, Santa Fe, New Mexico, Feb. 1−4, 2004; paper 196.

(37) Xiao, R. F.; Ng, L. C.; Yu, P.; Wong, K. L. Preparation of Crystalline Beta Barium Borate (β-BaB_2O_4) Thin Films by Pulsed Laser Deposition. *Appl. Phys. Lett.* **1995**, *67*, 305.

(38) Li, W.; Guler, U.; Kinsey, N.; Naik, G. V.; Boltasseva, A.; Guan, J.; Shalaev, V. M.; Kildishev, A. V. Refractory Plasmonics with

DOI: 10.1021/acsnano.8b06308
ACS Nano 2019, 13, 1213−1222

Titanium Nitride: Broadband Metamaterial Absorber. *Adv. Mater.* **2014**, *26*, 7959−7965.
(39) Lassiter, J. B.; Chen, X.; Liu, X.; Ciracì, C.; Hoang, T. B.; Larouche, S.; Oh, S. H.; Mikkelsen, M. H.; Smith, D. R. Third-harmonic Generation Enhancement by Film-coupled Plasmonic Stripe Resonators. *ACS Photonics* **2014**, *1*, 1212−1217.
(40) Moreau, A.; Ciraci, C.; Mock, J. J.; Hill, R. T.; Wang, Q.; Wiley, B. J.; Chilkoti, A.; Smith, D. R. Controlled-reflectance Surfaces with Film-coupled Colloidal Nanoantennas. *Nature* **2012**, *492*, 86−89.
(41) Viezbicke, B. D.; Patel, S.; Davis, B. E.; Birnie, D. P. Evaluation of the Tauc Method for Optical Absorption Edge Determination: ZnO Thin Films as a Model System. *Phys. Status Solidi B* **2015**, *252*, 1700−1710.
(42) Inbar, I.; Cohen, R. E. Comparison of the Electronic Structures and Energetics of Ferroelectric $LiNbO_3$ and $LiTaO_3$. *Phys. Rev. B: Condens. Matter Mater. Phys.* **1996**, *53*, 1193.
(43) Piskunov, S.; Heifets, E.; Eglitis, R. I.; Borstel, G. Bulk Properties and Electronic Structure of $SrTiO_3$, $BaTiO_3$, $PbTiO_3$ Perovskites: an *Ab Initio* HF/DFT Study. *Comput. Mater. Sci.* **2004**, *29*, 165−178.
(44) Wang, F. X.; Rodríguez, F. J.; Albers, W. M.; Ahorinta, R.; Sipe, J. E.; Kauranen, M. Surface and Bulk Contributions to The Second-order Nonlinear Optical Response of a Gold Film. *Phys. Rev. B: Condens. Matter Mater. Phys.* **2009**, *80*, 233402.
(45) Baudrier-Raybaut, M.; Haidar, R.; Kupecek, Ph.; Lemasson, Ph.; Rosencher, E. Random Quasi-phase-matching in Bulk Polycrystalline Isotropic Nonlinear Materials. *Nature* **2004**, *432*, 374−376.
(46) Arie, A.; Voloch, N. Periodic, Quasi-periodic, and Random Quadratic Nonlinear Photonic Crystals. *Laser Photonics Rev.* **2010**, *4*, 355−373.
(47) Vidal, X.; Martorell, J. Generation of Light in Media with a Random Distribution of Nonlinear Domains. *Phys. Rev. Lett.* **2006**, *97*, No. 013902.
(48) Zeng, Y.; Hoyer, W.; Liu, J.; Koch, S. W.; Moloney, J. V. Classical Theory for Second-harmonic Generation from Metallic Nanoparticles. *Phys. Rev. B: Condens. Matter Mater. Phys.* **2009**, *79*, 235109.
(49) Luong, N.; Cheng, C. W.; Shih, M. H.; Kuang, W. Phase Matching for Surface Plasmon Enhanced Second Harmonic Generation in a Gold Grating Slab. *Appl. Phys. Lett.* **2012**, *100*, 181107.
(50) Capretti, A.; Wang, Y.; Engheta, N.; Dal Negro, L. Comparative Study of Second-Harmonic Generation from Epsilon-Near-Zero Indium Tin Oxide and Titanium Nitride Nanolayers Excited in the Near-Infrared Spectral Range. *ACS Photonics* **2015**, *2*, 1584−1591.
(51) Linnenbank, H.; Grynko, Y.; Förstner, J.; Linden, S. Second Harmonic Generation Spectroscopy on Hybrid Plasmonic/dielectric Nanoantennas. *Light: Sci. Appl.* **2016**, *5*, No. e16013.
(52) Metzger, B.; Hentschel, M.; Schumacher, T.; Lippitz, M.; Ye, X.; Murray, C. B.; Knabe, B.; Buse, K.; Giessen, H. Doubling the Efficiency of Third Harmonic Generation by Positioning ITO Nanocrystals into the Hot-spot of Plasmonic Gap-antennas. *Nano Lett.* **2014**, *14*, 2867−2872.
(53) Nikogosyan, D. N. *Nonlinear Optical Crystals: A Complete Survey*; Springer-Science, 2010; p 199.
(54) Shimizu, T.; Katayama, K.; Kiguchi, T.; Akama, A.; Konno, T. J.; Funakubo, H. Growth of Epitaxial Orthorhombic $YO_{1.5}$-substituted HfO_2 Thin Film. *Appl. Phys. Lett.* **2015**, *107*, No. 032910.
(55) Riedel, S.; Polakowski, P.; Müller, J. A. Thermally Robust and Thickness Independent Ferroelectric Phase in Laminated Hafnium Zirconium Oxide. *AIP Adv.* **2016**, *6*, No. 095123.
(56) Xu, J.; Semin, S.; Niedzialek, D.; Kouwer, P. H. J.; Fron, E.; Coutino, E.; Savoini, M.; Li, Y.; Hofkens, J.; Uji-I, H.; Beljonne, D.; Rasing, T.; Rowan, A. E. Self-Assembled Organic Microfibers for Nonlinear Optics. *Adv. Mater.* **2013**, *25*, 2084−2089.
(57) Humlicek, J.; Nebojsa, A.; Hora, J.; Strasky, M.; Spousta, J.; Sikola, T. Ellipsometry and Transport Studies of Thin-film Metal Nitrides. *Thin Solid Films* **1998**, *332*, 25−29.

DOI: 10.1021/acsnano.8b06308
ACS Nano 2019, 13, 1213−1222